

See discussions, stats, and author profiles for this publication at: <https://www.researchgate.net/publication/263950218>

# Enhanced Photocatalytic Activity of Chemically Bonded TiO<sub>2</sub>/Graphene Composites Based on the Effective Interfacial Charge Transfer through the C–Ti Bond

ARTICLE in ACS CATALYSIS · JUNE 2013

Impact Factor: 9.31 · DOI: 10.1021/cs400080w

CITATIONS

74

READS

185

8 AUTHORS, INCLUDING:



**Shouqin Tian**

Wuhan University of Technology

28 PUBLICATIONS 395 CITATIONS

SEE PROFILE



**Dawen Zeng**

Huazhong University of Science and Technol...

132 PUBLICATIONS 2,110 CITATIONS

SEE PROFILE



**Wulin Song**

Huazhong University of Science and Technol...

67 PUBLICATIONS 682 CITATIONS

SEE PROFILE

# Enhanced Photocatalytic Activity of Chemically Bonded TiO<sub>2</sub>/Graphene Composites Based on the Effective Interfacial Charge Transfer through the C–Ti Bond

Qingwu Huang,<sup>†,§</sup> Shouqin Tian,<sup>‡</sup> Dawen Zeng,<sup>\*,†,‡</sup> Xiaoxia Wang,<sup>‡</sup> Wulin Song,<sup>§</sup> Yingying Li,<sup>||</sup> Wei Xiao,<sup>||</sup> and Changsheng Xie<sup>\*,‡</sup>

<sup>†</sup>State Key Laboratory of Materials Processing and Die & Mold Technology, <sup>‡</sup>Nanomaterials and Smart Sensors Research Lab (NSSRL), Department of Materials Science and Engineering, <sup>§</sup>Analytical and Testing Center of Huazhong University of Science and Technology, Huazhong University of Science and Technology, No. 1037, Luoyu Road, Wuhan 430074, People's Republic of China

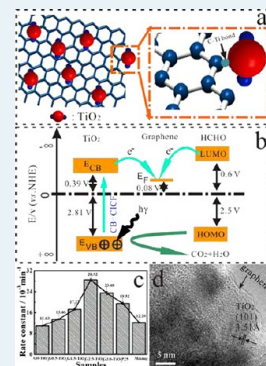
<sup>‡</sup>State Key Laboratory of Silicate Materials for Architectures, Wuhan University of Technology, No. 122, Luo-shi Road, Wuhan, 430070, People's Republic of China

<sup>||</sup>State Nuclear Power Research Institute, Beijing 100029, People's Republic of China

## Supporting Information

**ABSTRACT:** Recently, graphene-based semiconductor photocatalysts have attracted more attention because of their enhanced photocatalytic activity caused by interfacial charge transfer (IFCT). However, the effect of a chemical bond is rarely involved for the IFCT. In this work, TiO<sub>2</sub>/graphene composites with a chemically bonded interface were prepared by a facile solvothermal method using tetrabutyl orthotitanate (TBOT) as the Ti source. The chemically bonded TiO<sub>2</sub>/graphene composites effectively enhanced their photocatalytic activity in photodegradation of formaldehyde in air, and the graphene content exhibited an obvious influence on the photocatalytic activity. The prepared composite with 2.5 wt % graphene (G2.5-TiO<sub>2</sub>) showed the highest photocatalytic activity, exceeding that of Degussa P25, as-prepared pure TiO<sub>2</sub> nanoparticles, and the mechanically mixed TiO<sub>2</sub>/graphene (2.5 wt %) composite by a factor of 1.5, 2.6, and 2.3, respectively. The enhancement in the photocatalytic activity was attributed to the synergetic effect between graphene and TiO<sub>2</sub> nanoparticles. Other than the graphene as an excellent electron acceptor and transporter, the enhanced photocatalytic activity was caused by IFCT through a C–Ti bond, which markedly decreased the recombination of electron–hole pairs and increased the number of holes participating in the photooxidation process, confirmed by XPS analysis, the gaseous phase transient photocurrent response, electrochemical impedance spectroscopy, and photoluminescence spectra. This work about effective IFCT through a chemically bonded interface can provide new insights for directing the design of new heterogeneous photocatalysts, which can be applied in environmental protection, water splitting, and photoelectrochemical conversion.

**KEYWORDS:** chemical bonding, C–Ti bond, photocatalytic activity, interfacial charge transfer, gaseous phase photocurrent



## 1. INTRODUCTION

In recent years, semiconductor (SC) photocatalysis has emerged as an advanced green technology for environmental pollution purification.<sup>1</sup> In photocatalysis, photogenerated electrons and (or) holes involve mainly two processes. One is driving the photocatalytic reactions, and another is recombination and generation of heat, which is harmful to photocatalysis. Further studies indicate that only a small fraction of photogenerated carriers can successfully transfer to the interface to initiate redox reactions, so effective electron transfer at the SC surface has been widely acclaimed to be of great importance, which is a fundamental process relevant to photocatalytic applications.

To date, titania has proven to be the most suitable photocatalyst, largely due to its strong oxidizing power, biological and chemical inertness, and low cost.<sup>2</sup> Unfortunately, the rapid recombination rate of photogenerated electron–hole

pairs within TiO<sub>2</sub> results in its low quantum efficiency, thus limiting its practical application.<sup>3</sup> In the past decades, various strategies have been developed in an attempt to modify the photocatalytic process and improve the photocatalytic performance.<sup>2b,4</sup> In particular, carbon–titania hybrid materials have been receiving much attention as a new class of photocatalysts,<sup>5</sup> which could potentially offer desirable efficiency for separating electron–hole pairs.

Recently, owing to the high specific surface area and superior electron mobility of graphene, numerous efforts have been paid to combine graphene with semiconductor photocatalysts to enhance the catalytic performance.<sup>6</sup> It is believed that photoexcited electrons from TiO<sub>2</sub> transfer to nanocarbons,

Received: January 31, 2013

Revised: May 7, 2013

such as carbon nanotubes or graphene, and hinder the recombination process, thereby enhancing the oxidative reactivity.<sup>7</sup> Further studies indicate that the interaction between graphene and  $\text{TiO}_2$  can significantly determine the interfacial electron transfer properties, which is a key issue for photocatalytic activity. Dong et al.<sup>8</sup> find that a RGO/ $\text{TiO}_2$  composite will significantly increase the photovoltaic response and significantly prolong the mean lifetime of electron–hole pairs compared with pure  $\text{TiO}_2$ , which is experimentally supported by a transient photovoltage (TPV) result. Li et al.<sup>7c</sup> reported chemically bonded P25-graphene composite as a high-performance photocatalyst for degradation of methylene blue. In Zhang and Wang's report,<sup>9</sup> P25/RGO composite with the most intensive interaction fabricated by a hydrothermal method shows the highest  $\text{H}_2$  evolution activity; however, it has rarely been reported that chemical bonding plays a critical role on the interfacial charge transfer (IFCT) and photocatalytic performance, especially compared with mechanically mixed semiconductor/graphene without a chemically bonded interface.

In this paper, we demonstrate that  $\text{TiO}_2$ /graphene composites with a C–Ti chemically bonded interface were prepared by a facile solvothermal method using TBOT as the Ti source. XPS analysis confirmed the existence of a chemical C–Ti bond between the graphene and  $\text{TiO}_2$  nanoparticles. What's more, chemical bonding is of great importance for the efficiency of photoinduced interfacial electron transfer. Because of the photoinduced chemically bonded interfacial charge transfer (CB-IFCT),  $\text{TiO}_2$ /graphene nanocomposites with a C–Ti bond exhibit exceptional photocatalytic reactivity toward removing HCHO in air compared with pure  $\text{TiO}_2$  and the corresponding mechanical mixed sample (without chemical bonding). It is proposed that the photoinduced CB-IFCT can effectively enhance photocatalytic reactivity by decreasing the possibility of recombination of electron–hole pairs and increasing the number of holes participating in the photo-oxidation process.

## 2. EXPERIMENTAL SECTION

**2.1. Sample Preparation.** All chemicals used in this study were analytical grade and were used without further purification. Distilled water was used in all experiments. The graphene used in all experiments was prepared on the basis of Stride's reports.<sup>10</sup> In a typical preparation procedure for graphene/ $\text{TiO}_2$  nanocomposites, 0.02 mol of tetrabutyl orthotitanate (TBOT) was dissolved into 30 mL of ethanol, and then this TBOT solution was added dropwise under magnetic stirring to 10 mL of graphene water suspension, which contained a specific amount of the graphene. The designed mass ratio of graphene to titania was 0, 0.5, 1.5, 2.5, and 3.0 wt %, and the corresponding final products are denoted as Gx- $\text{TiO}_2$ , where x is 0, 0.5, 1.5, 2.5, and 3.0, respectively. After stirring for another 120 min, the mixed suspension was transferred to a 70 mL Teflon-lined autoclave and maintained at 200 °C for 10 h. The obtained white or black–white precipitates were collected and washed thoroughly with distilled water and absolute ethanol for several cycles and then dried in vacuum at 80 °C for 12 h to get the Gx- $\text{TiO}_2$  nanocomposites. For comparison, a sample with a graphene loading of about 2.5 wt % was also prepared by a simple mechanical mixing of G0- $\text{TiO}_2$  and graphene, which is noted hereafter as “Mixing”.

**2.2. Characterization.** Powder X-ray diffraction (XRD) patterns were obtained on a Philips X'Pert Pro X-ray diffractometer (PANalytical, Holland) with Cu K $\alpha$  radiation

( $\lambda = 0.15418$  nm) at a scan rate ( $2\theta$ ) of  $0.05^\circ \text{ s}^{-1}$ . The accelerating voltage and the applied current were 40 kV and 80 mA, respectively. Raman spectra were recorded at room temperature using a micro-Raman spectrometer (Horiba Jobin Yvon, LabRAM HR800) in the backscattering geometry with a 488 nm laser as an excitation source. Transmission electron microscope (TEM) measurements were performed with a JEM-2100F STEM microscope operating at 200 kV. X-ray photoelectron spectroscopy (XPS) measurements were carried out with a VG Multilab 2000 spectrometer employing Mg K $\alpha$  radiation. UV–visible absorbance spectra were obtained for the dry-pressed disk samples with a UV–visible spectrophotometer (Lambda 35, PerkinElmer, America).  $\text{BaSO}_4$  was used as a reflectance standard in a UV–visible diffuse reflectance experiment. The thermogravimetric analysis differential thermal analysis (TG-DTA) was carried out using a Perkin-Elmer Pyris Diamond analyzer in air at a heating rate of  $10^\circ \text{ C min}^{-1}$ . Photoluminescence (PL) emission spectra were acquired under excitation at 325 nm using an Edinburgh Instruments PLSP920 spectrometer.

For the electrochemical impedance spectroscopy (EIS) measurement, the as-prepared photocatalyst powders were fixed to the film electrodes by the following method: First, the powders and ethanol were mixed homogeneously (200 mg/mL), and the obtained paste was then spread on the conducting fluorine-doped  $\text{SnO}_2$  glass substrate (FTO, with a sheet resistance of  $15 \Omega$ ) with a glass rod. Finally, the resultant films with a  $\sim 2 \mu\text{m}$  thickness and  $2 \text{ cm}^2$  active areas were calcinated at 450 °C for 2 h in inert atmosphere to achieve good electronic contact between the photocatalyst and FTO glass. The EIS measurements were carried out on an IM6eX electrochemical workstation (Zahner, INC. Germany) by using three-electrode cells. EIS measurements were carried out in  $\text{H}_2\text{SO}_4$  solution (25%) by using a three-electrode system. The resultant electrode served as the working electrode, with a platinum wire as the counter electrode and a Ag/AgCl (saturated KCl) electrode as the reference electrode. The measurement was performed in the presence of a 2.5 mM  $\text{K}_3[\text{Fe}(\text{CN})_6]/\text{K}_4[\text{Fe}(\text{CN})_6]$  (1:1) mixture as a redox probe in 0.1 M KCl solution. The impedance spectra were recorded under an AC perturbation signal of 5 mV over the frequency range of 1 MHz to 10 mHz at 0.5 V.

For the gaseous phase photocurrent measurement under HCHO gas atmosphere, the as-prepared photocatalyst powders were fixed to the film electrodes by the following method: First, the powders and ethanol were mixed homogeneously (200 mg/mL), and the obtained paste was then spread on thin, flat alumina ( $\sim 6 \times 8 \text{ mm}$ ), which was preprinted with the Au interdigital electrode. The condition of photocurrent measurement was kept the same as gaseous photocatalytic degradation experiments (200 ppm HCHO gas and  $36 \text{ W/m}^2$  UV irradiation) and the bias voltage was 5 V.

**2.3. Photocatalytic Activity.** Photocatalytic activity of the samples was evaluated by degrading  $\sim 200$  ppm HCHO under irradiation of a UV (365 nm) LED light at ambient temperature with a 1 L reactor. The powder photocatalysts were coated onto a square groove ( $5 \times 5 \text{ cm}$ ), and dried in an oven at 80 °C for 2 h. The weight of the photocatalysts used for each experiment was kept at about 0.05 g. After the square groove coated with photocatalyst powders was placed into the reactor, HCHO gas ( $\sim 200$  ppm) was passed through the reactor and reached adsorption–desorption equilibrium with the catalyst before light irradiation. The initial temperature was  $25 \pm 1^\circ \text{ C}$ .



Finally, a 2.8 W UV LED array lamp (1 cm above the groove) was switched on to trigger the photocatalytic reaction. The measured UV intensity was  $\sim 36 \text{ W/m}^2$ . The analysis for the HCHO concentration and carbon dioxide in the reactor was performed online with a photoacoustic field gas-monitor (INNOVA Air Tech Instruments, model 1412). Each set of experiments was followed by 60 min under UV irradiation.

### 3. RESULTS AND DISCUSSION

**3.1. Enhanced Photocatalytic Properties.** To analyze the application potential of graphene/TiO<sub>2</sub> nanocomposites in volatile organic compound (VOC) gas purification, photocatalytic degradation was determined to select HCHO gas as the target gas. The photocatalytic activities of the as-prepared graphene/TiO<sub>2</sub> nanocomposites were evaluated by the oxidation of 200 ppm HCHO gas in air. Note that dark conditions without light illumination or illumination in the absence of catalyst did not result in the photocatalytic decomposition of HCHO. Therefore, the presence of both illumination and catalyst was necessary for efficient degradation. These results clearly indicated that the decomposition of HCHO in air was caused by photocatalytic reactions on graphene/TiO<sub>2</sub> composite powders under UV illumination.

The kinetics of the degradation reaction was fitted to a pseudo-first-order reaction, and a much larger apparent rate constant ( $\kappa$ ) for the hybrid was quantitatively evaluated, as Figure 1 shows. Without graphene, the sample G0-TiO<sub>2</sub> shows

by 1.5 times, which indicates the excellent photocatalytic activity of Gx-TiO<sub>2</sub> composite. The Mixing sample shows a  $\kappa$  value only slightly higher than that of the G0-TiO<sub>2</sub> sample, which indicates that simply mechanically adding graphene without a chemically bonded interface has a small effect on photocatalytic activity. In addition, even though the Mixing and G2.5-TiO<sub>2</sub> samples have the same graphene loading, their photocatalytic activities show a great difference, by a factor of  $\sim 2.3$ . This difference in the photocatalytic activity means that the interaction state between graphene and TiO<sub>2</sub> nanoparticles has a vital effect on the photocatalytic activity.

For the practical application of photocatalysts, the mineralization ratio in the catalysis process and the stability of photocatalyst are two key issues. The photocatalytic process is complex, and many intermediate products are produced, especially when the initial pollutant is complicated. Some intermediate products may be more harmful to human health than the initial pollutant, so a thorough decomposition of the pollutant is necessary. Fortunately, the concentration of HCHO and CO<sub>2</sub> decreases and increases linearly, respectively, for all the prepared photocatalysts. Moreover, the concentration of the produced carbon dioxide is about the same as that of the decomposed HCHO (shown in Figure 2a), suggesting that HCHO is completely degraded to CO<sub>2</sub> by the prepared TiO<sub>2</sub>/graphene photocatalysts.

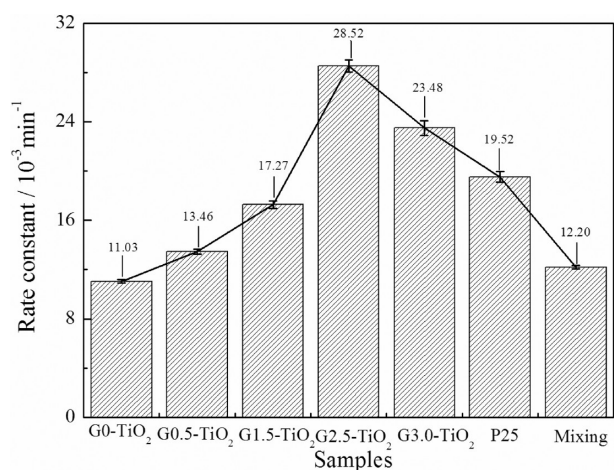


**Figure 1.** The photocatalytic activity ( $\kappa$ ) of Gx-TiO<sub>2</sub> composites ( $x = 0, 0.5, 1.5, 2.5$ , and  $3.0$ ), P25, and Mixing samples.

good photocatalytic activity, and its  $\kappa$  reaches  $11.03 \times 10^{-3} \text{ min}^{-1}$ . Even when the loading amount of graphene (0–3.0 wt %) is low, the adding graphene exhibits a significant influence on the photocatalytic activity of the graphene/TiO<sub>2</sub> nanocomposites. Especially, the photocatalytic activity increases significantly with increasing loaded graphene content, and the  $\kappa$  reaches the highest value of  $28.52 \times 10^{-3} \text{ min}^{-1}$  at 2.5 wt % graphene (G2.5-TiO<sub>2</sub>). In this regard, the photocatalytic activity exceeds that of pure TiO<sub>2</sub> by 2.6 times. However, when further increasing the graphene content to 3.0 wt %, its  $\kappa$  value decreases to  $23.48 \times 10^{-3} \text{ min}^{-1}$ . For comparison, the photocatalytic activity of P25 (Degussa, TiO<sub>2</sub>) and Mixing was also carried out, with respective  $\kappa$  values of  $19.52 \times 10^{-3} \text{ min}^{-1}$  and  $12.2 \times 10^{-3} \text{ min}^{-1}$ , under the same test conditions. The highest photocatalytic activity (G2.5-TiO<sub>2</sub>) exceeds that of P25

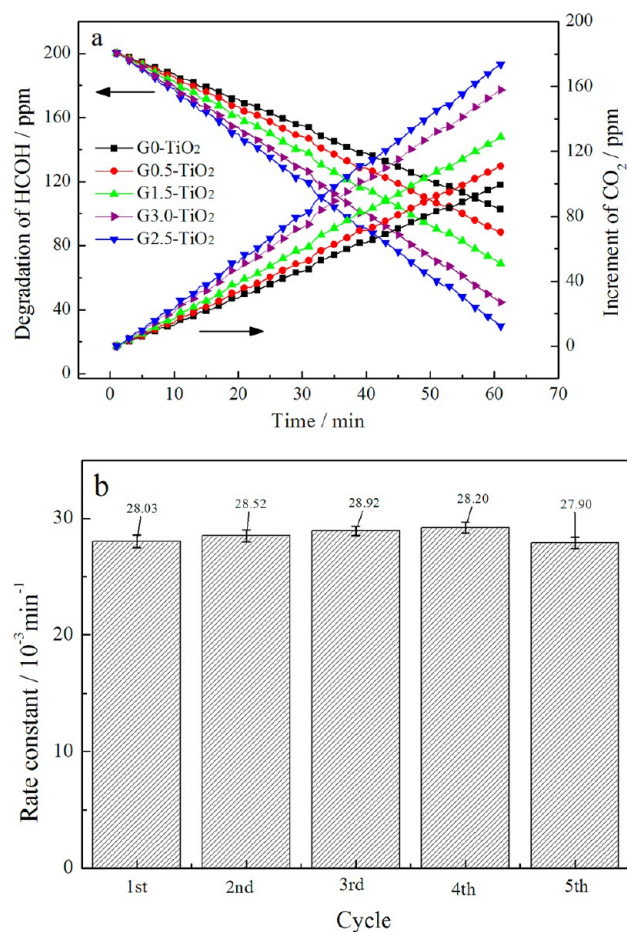


**Figure 2.** (a) The degradation curves of HCHO and increase of CO<sub>2</sub> by Gx-TiO<sub>2</sub> composite ( $x = 0, 0.5, 1.5, 2.5$ , and  $3.0$ ) and (b) the stability test of the G2.5-TiO<sub>2</sub> photocatalyst.

The stability of the photocatalyst is another important practical issue. The intermediate products are usually adsorbed on the surface-active position of the photocatalyst. The photocatalytic activity will decrease dramatically after several cycles of usage. Figure 2b shows the photocatalytic stability of G2.5-TiO<sub>2</sub> photocatalysts for five cycles of usage. The  $\kappa$  value rarely stayed the same in the first four cycles and decreased only slightly in the fifth cycle.

The excellent mineralization efficiency and high photocatalytic stability demonstrate the good practical application potential of the prepared TiO<sub>2</sub>/graphene nanocomposite. The excellent photocatalytic activity of as-prepared TiO<sub>2</sub>/graphene nanocomposites is interesting, and detailed characterizations were carried out to reveal the photocatalysis mechanism.

### 3.2. Structure and Morphology of TiO<sub>2</sub>/Graphene Nanocomposites.

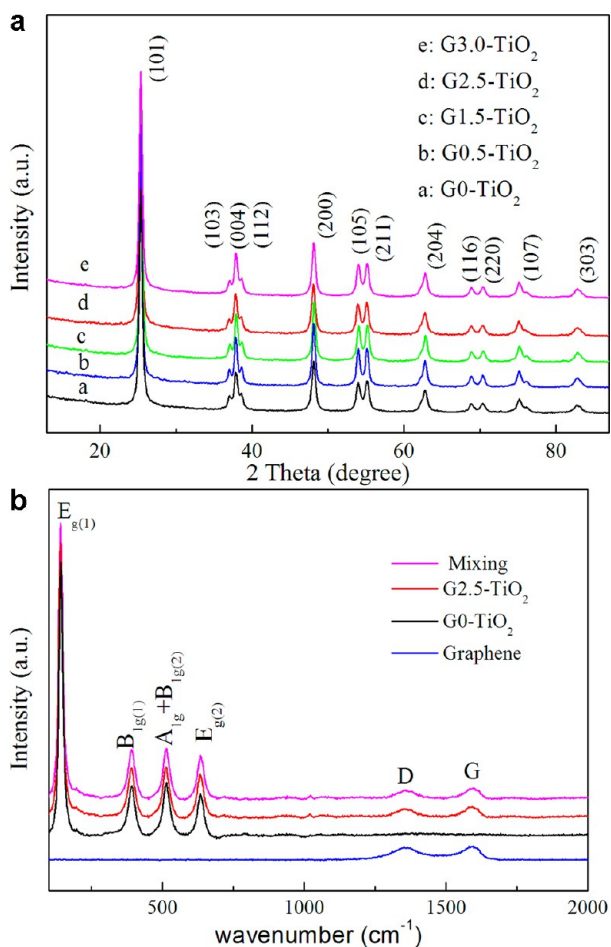


**Figure 3.** (a) XRD patterns of TiO<sub>2</sub>/graphene nanocomposites and (b) Raman spectra of G2.5-TiO<sub>2</sub>, Mixing, G0-TiO<sub>2</sub>, and pure graphene.

TiO<sub>2</sub>/graphene nanocomposites synthesized with different contents of graphene compared with pure TiO<sub>2</sub>. The present peaks clearly represent the formation of anatase crystallites (JCPDS no. 01-089-4921). Otherwise, no apparent peaks for graphene were observed. The trace amount of loaded graphene with low atomic number ( $Z = 6$ ) cannot be resolved by XRD;<sup>11</sup> however, the existence of graphene can be clearly elucidated by Raman analysis, as discussed next.

The local structure of the TiO<sub>2</sub>/graphene composite was investigated by comparing its Raman spectra with those of pure TiO<sub>2</sub> and graphene (Figure 3b). The four bands located at around 141 (E<sub>g(1)</sub>), 391 (B<sub>1g(1)</sub>), 514 (A<sub>1g</sub> + B<sub>1g(2)</sub>), and 634 cm<sup>-1</sup> (E<sub>g(2)</sub>) are characteristic for pure anatase TiO<sub>2</sub> (G0-TiO<sub>2</sub>, Figure 3b).<sup>12</sup> The two typical bands located at around 1355 (D band) and 1595 cm<sup>-1</sup> (G band) correspond to graphene (Figure 3b).<sup>13</sup> As for the Mixing and G2.5-TiO<sub>2</sub> (Figure 3b), all the Raman bands for anatase TiO<sub>2</sub> and graphene are basically retained. In addition, a smaller intensity ratio of the D band to G band was found in Mixing ( $I_D/I_G = 0.75$ ) and G2.5-TiO<sub>2</sub> ( $I_D/I_G = 0.79$ ) compared with pure graphene ( $I_D/I_G = 0.94$ ), which can be assigned to lower defects and disorder of the graphene structures.<sup>11a</sup> This demonstrated that TiO<sub>2</sub> and graphene existed in Mixing and G2.5-TiO<sub>2</sub>.

The SEM images of the as-prepared Gx-TiO<sub>2</sub> nanocomposite are shown in Figure 4. The pure TiO<sub>2</sub> nanoparticles (G0-TiO<sub>2</sub>) were evenly distributed (in Figure 4a). After adding graphene, the TiO<sub>2</sub> nanoparticles were located or wrapped by graphene nanosheets (in Figure 4b–d). The external morphology and microstructures of the TiO<sub>2</sub>/graphene nanocomposites with 2.5 wt % graphene were further studied by TEM (Figure 5). Because of interfacial interactions and preferential heterogeneous nucleation,<sup>6c</sup> numerous TiO<sub>2</sub> nanocrystals were densely deposited onto the graphene sheets (in Figure 5a, b). The corresponding HRTEM image (in Figure 5d) showed clear lattice fringes, which allowed for the identification of crystallographic spacing. The fringe spacing of  $\sim 3.51$  Å matched that of the (101) crystallographic plane of anatase TiO<sub>2</sub>. From the inset of Figure 5d, the ( $\bar{1}01$ ) facet was also observed. According to the crystallographic knowledge and imaging theory of TEM, the exposed facet (010) of TiO<sub>2</sub> was perpendicular to these two crystal facets. In addition, the edge of the graphene can also be observed and indicated in Figure 5d. This suggested that the exposed facet (010) of TiO<sub>2</sub> was attached to the surface of graphene and, thus, probably forming an interface between TiO<sub>2</sub> and graphene. In addition, the (010) facet with more Ti atoms exhibited a higher surface energy than the (101) plane,<sup>14</sup> indicating that there probably was an interaction between the Ti atoms and graphene.

To study the interaction between graphene and TiO<sub>2</sub> in Gx-TiO<sub>2</sub>, XPS analysis was utilized. Figure 6a shows the high-resolution XPS spectra of C 1s region for the Mixing sample. The binding energy of 284.8 eV was a typical peak position for graphite carbon, which demonstrated the sp<sup>2</sup>-hybridized carbon in the graphene state.<sup>11a</sup> Furthermore, the deconvoluted peaks centered at the binding energy of 285.9 and 289.0 eV were attributed to the C–O and C=O oxygen-containing carbonaceous bands.<sup>5j</sup> C 1s spectra for the as-prepared G2.5-TiO<sub>2</sub> composite are shown in Figure 6b. Two distinct peaks at 284.7 and 286.0 eV corresponded to graphitic carbon in graphene and oxygenated carbons in the C–O bond. In addition, an additional shoulder peak located at 281.2 eV was found, which was usually assigned to the formation of a chemical bond between a carbon atom and a titanium atom in the lattice of TiO<sub>2</sub>, which resulted in formation of C–Ti bonds.<sup>15</sup> Furthermore, lower amounts of the oxygen-containing carbonaceous bands were detected in the carbon peak of G2.5-TiO<sub>2</sub> because the peak area ratio of C–O bonds was obviously decreased and the peak of C=O was not observed in Figure 6b, indicating fewer oxygen deficiencies.

Formation of the C–Ti bond also can be examined and confirmed by analysis of the Ti (2p) core level of the XPS



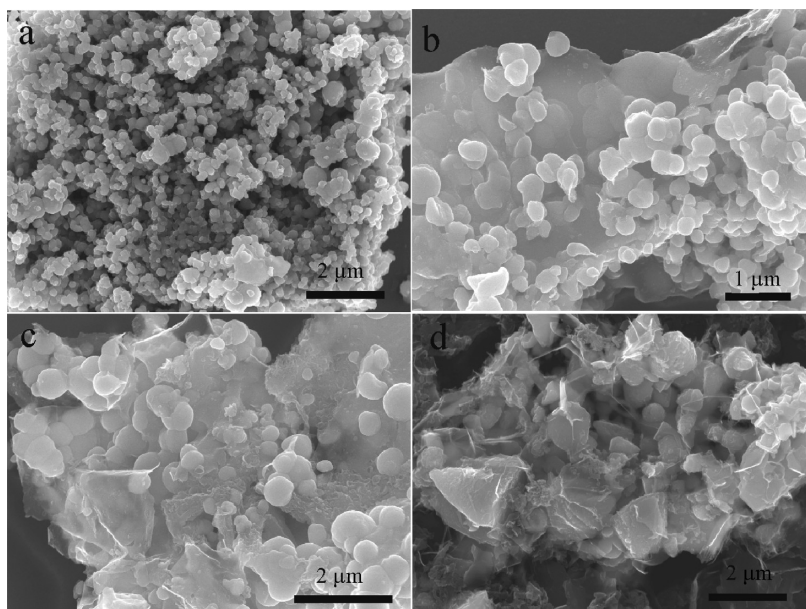


**Figure 4.** SEM images of  $G_x\text{-TiO}_2$  nanocomposite, where  $x = 0$  (a), 0.5 (b), 1.5 (c), and 2.5(d).

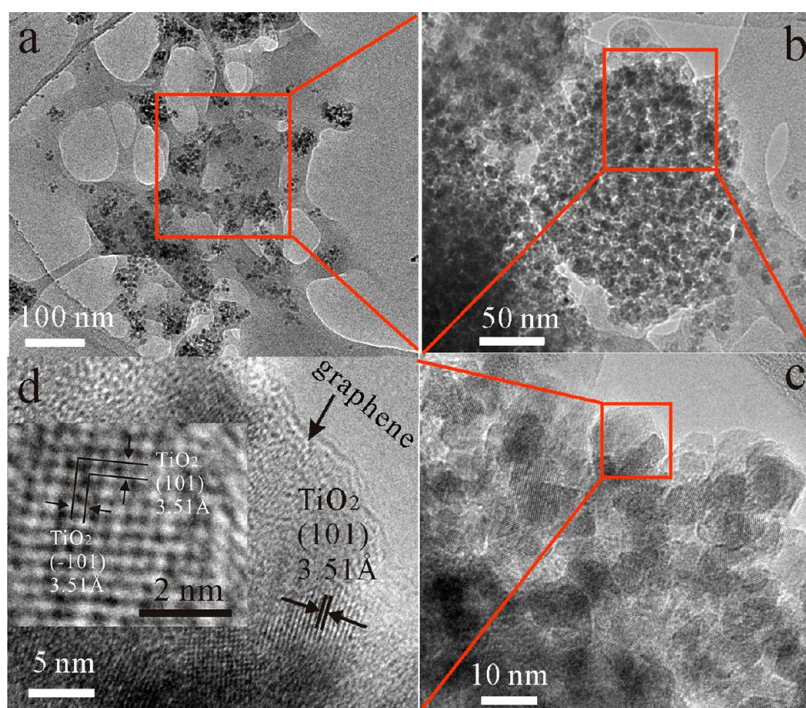


**Figure 5.** (a, b) TEM and (c, d) HRTEM images of  $G_{2.5}\text{-TiO}_2$  nanocomposite.

spectra, as shown in Figure 6c, d. Figure 6c shows XPS spectra for the Mixing sample at the Ti (2p) binding energy regions. The bands located at binding energies of 458.8 and 464.6 eV were assigned to the O–Ti bond in  $\text{TiO}_2$ .<sup>16</sup> In Figure 6d, in addition to the two characteristic peaks of  $\text{TiO}_2$  at 458.8 eV (Ti 2p<sub>3/2</sub>) and 464.6 eV (Ti 2p<sub>1/2</sub>), two other weak peaks centered at 455.1 and 461.1 eV (relating to the Ti 2p<sub>3/2</sub> and 2p<sub>1/2</sub>) were found and probably result from a C–Ti bond between  $\text{TiO}_2$  and graphene in the  $G_{2.5}\text{-TiO}_2$  composite. This demonstrated that the C–Ti chemical bond was present in  $G_{2.5}\text{-TiO}_2$  and absent in the Mixing sample. In addition, the formation of the C–Ti chemical bond was also confirmed by the calculation results in Figures S1 and S2 of the Supporting Information. As

can be seen, the (010) facet of  $\text{TiO}_2$  with a higher energy surface and more Ti atoms can adsorb graphene easily, and thus, the C–Ti chemical bond can be formed easily between the (010) facet of  $\text{TiO}_2$  and graphene. Furthermore, the DOS of anatase (010)/graphene in Figure S3 of the Supporting Information shows that the DOS profiles of Ti and C coincide with each other, further suggesting the formation of the chemical bond between Ti and C atoms.

TG-DTA analysis was carried out to further confirm the chemical bonding by the carbon atom in the  $G_{2.5}\text{-TiO}_2$  composite. Figure 7 shows the TG-DTA curve of  $G_{2.5}\text{-TiO}_2$  and mechanically mixed  $\text{TiO}_2$ /graphene (with 2.5% graphene loading) composite, which were performed in an air

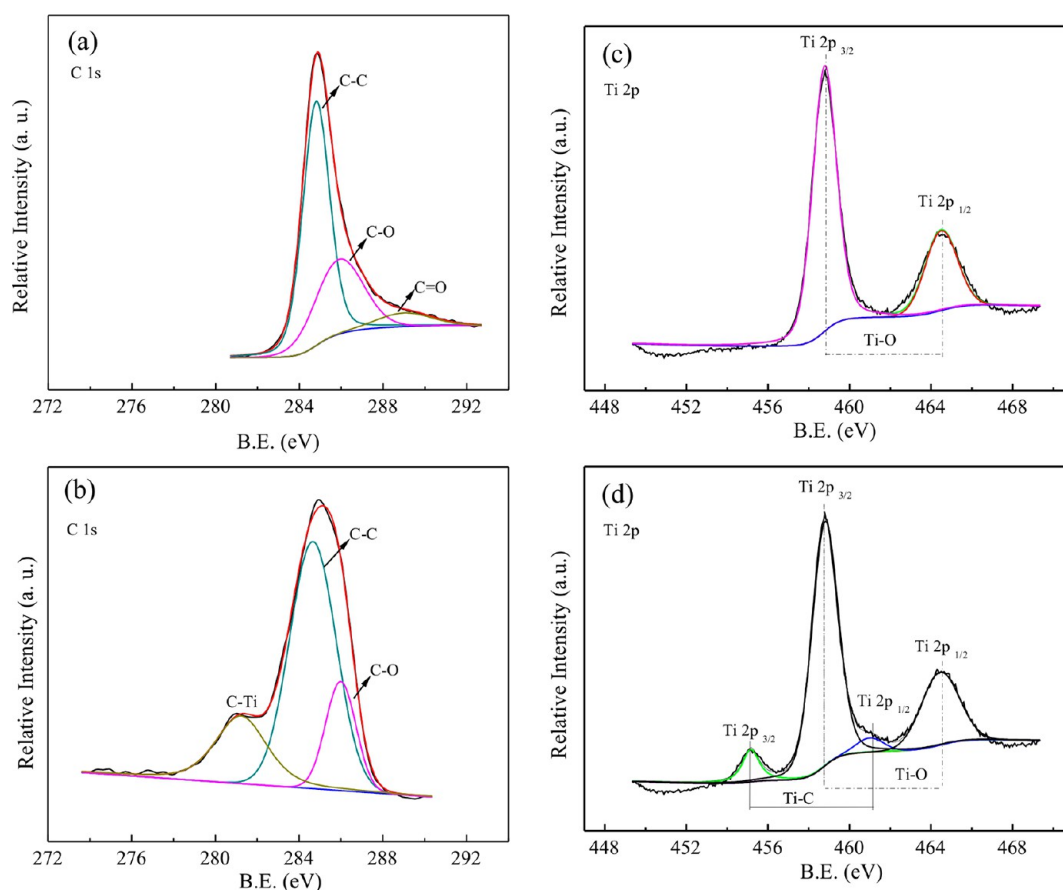


**Figure 6.** The C 1s (a, b) and Ti 2p (c, d) XPS spectra of mechanically mixed (a, c) and chemically bonded (b, d)  $\text{TiO}_2$ /graphene nanocomposites.

atmosphere with a heating rate of  $10\text{ }^\circ\text{C min}^{-1}$ . With increasing temperature, the mechanically mixed  $\text{TiO}_2$ /graphene showed a gradual mass loss until  $\sim 400^\circ\text{C}$ , and a very sharp exothermic peak at  $427^\circ\text{C}$  in the DTA curve (Figure 7b), which was attributed to the combustion of graphene layers. In contrast, the  $\text{G2.5-TiO}_2$  composite exhibited a later onset of weight loss than the mechanically mixed  $\text{TiO}_2$ /graphene composite and showed an obvious exothermic peak centered at  $533^\circ\text{C}$  (Figure 7a). This suggests that the thermal stability of the nanocomposite samples was enhanced, with the graphene nanosheets being stabilized by the deposited  $\text{TiO}_2$  nanoparticles as a result of the strong chemical coupling between them.<sup>17</sup> Likewise, this result proved that there was a C–Ti bond in the  $\text{G2.5-TiO}_2$  composite, in line with the above results.

The optical properties of the as-prepared  $\text{TiO}_2$ /graphene nanocomposites were measured by UV–vis diffuse reflectance spectra (in Supporting Information Figure S4a). All of these samples displayed the typical absorption with an intense transition in the UV region of the spectra, which was assigned to the intrinsic band gap absorption of  $\text{TiO}_2$  due to the electron transitions from the valence band to conduction band ( $\text{O}_{2p} \rightarrow \text{Ti}_{3d}$ ).<sup>18</sup> The  $\text{TiO}_2$ /graphene nanocomposites exhibited increasing absorption in the visible region after adding graphene. In line with the previous reports,<sup>7c</sup> a red shift to higher wavelength in the absorption edge of  $\text{Gx-TiO}_2$  composites has been observed, indicating a narrowing of the band gap of  $\text{Gx-TiO}_2$ . However, it was difficult to determine the value for such a red shift. A plot of the transformed Kubelka–Munk function dependent on the energy of light is shown in Supporting Information Figure S4b. The roughly estimated band gaps were

2.91, 2.94, 3.00, 2.94, and 3.02 eV for  $\text{G3.0-TiO}_2$ ,  $\text{G2.5-TiO}_2$ ,  $\text{G1.5-TiO}_2$ ,  $\text{G0.5-TiO}_2$ , and pure  $\text{TiO}_2$ , respectively. This red shift could be attributed to the chemical bonding between  $\text{TiO}_2$  and the specific sites of GO,<sup>7c</sup> which was consistent with the DOS result in Figure S3. In addition, there was an obvious decrease in UV light absorption for  $\text{Gx-TiO}_2$  compared with  $\text{G0-TiO}_2$ , which was in a good agreement with the previous reports.<sup>9</sup>

### 3.3. Mechanism of Enhanced Photocatalytic Activity.

On the basis of the above characterization results, the mechanism of enhanced photocatalytic activity could be attributed mainly to chemically bonded interfacial contact between  $\text{TiO}_2$  and graphene. Charge carrier transfer plays a pivotal role in photocatalytic processes, for once electron–hole pairs are generated by light excitation, most of them recombine, generating heat, and only a small fraction can successfully transfer to the interface to initiate redox reactions. It is reported that the factors affecting the efficiency of the electron transfer property includes the nanoparticles' surface,<sup>19</sup> size,<sup>20</sup> and morphology.<sup>21</sup> As for graphene-based photocatalysts, the enhanced carrier transfer property is contributed mainly by the enhanced special charge transportation properties of graphene.<sup>7c,22</sup> In addition, the interaction extent between graphene and semiconductor nanoparticles determines the electron transportation, which further determines the photocatalytic activity.<sup>9</sup> Our previous work about graphene/ $\text{BiOCl}$  photocatalyst reveals that the formation of C–Bi bond contributes much to the photocatalytic performance.<sup>11a</sup> Herein, we propose an effective chemically bonded interfacial charge

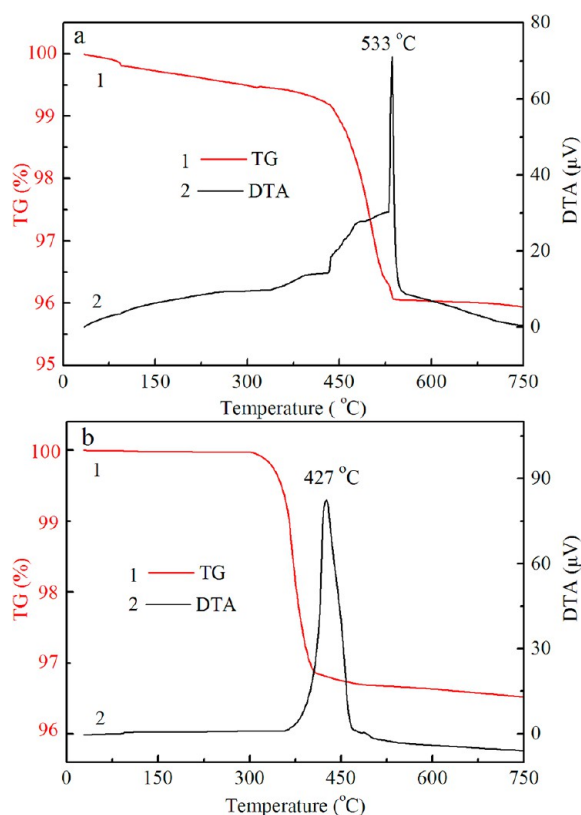


**Figure 7.** The TG-DTA curves of chemically bonded (a) and mechanically mixed (b)  $\text{TiO}_2$ /graphene nanocomposites.

transfer (CB-IFCT) to explain the enhanced photocatalytic activity of the  $\text{TiO}_2$ /graphene composite.<sup>11a,23</sup>

This is attributed to the mechanical mixing process not being able to create effective interfacial contact between  $\text{TiO}_2$  and graphene, whereas the  $\text{TiO}_2$ /graphene composite with chemical bonding causes an intimate interaction between the  $\text{TiO}_2$  nanoparticles and graphene nanosheets (illustrated in Figure 8a).<sup>22a,24</sup> In this regard, the graphene loading with intimate chemical bonding can efficiently facilitate the interfacial electron transfer and electron–hole separation.  $\text{TiO}_2$  has a high potential of the conduction band bottom (2.81 eV vs NHE, normal hydrogen electrode),<sup>25</sup> so the free electrons have powerful reducibility. Oxygen molecules adsorbed on the  $\text{TiO}_2$  surface could react with the free electrons. Thereby, a depletion layer is created with low conductivity near the surface.<sup>26</sup> Within  $\text{TiO}_2$  material, the CB electrons have to travel through the grain boundaries (GB). Thus, when a potential barrier is formed at the GB regions, the mobility of electron carriers could be limited.<sup>27</sup> In other words, the electrons that transfer from one  $\text{TiO}_2$  grain to the neighbored one should get through the potential barrier, so if  $\text{TiO}_2$  and graphene are chemically coupled, they can decrease the potential barrier at the GB regions. The chemical binding could provide a good spatial condition for charge transport from  $\text{TiO}_2$  to graphene via the interfaces; however, the mechanical mixing could not provide an intimate spatial condition for charge transport.

For the  $\text{TiO}_2$  materials, the reported energy level<sup>25</sup> of the valence band (VB) and conduction band (CB) is 2.81 and  $-0.39$  V vs NHE (normal hydrogen electrode), respectively. The calculated Fermi energy level of graphene is  $-0.08$  V vs NHE,<sup>28</sup> so it is energetically feasible that the photogenerated electron on the CB of  $\text{TiO}_2$  can transfer to graphene (as shown

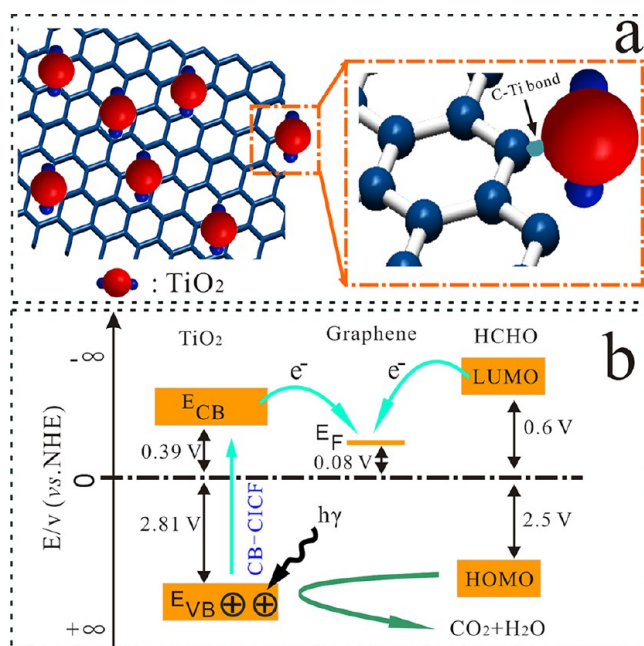
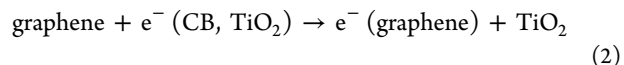
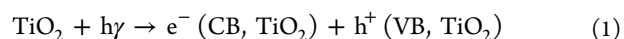


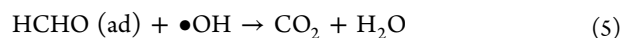
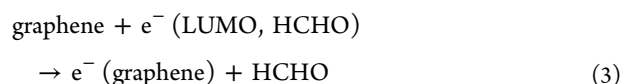
**Figure 8.** Schematic illustrations for an effective IFCT effect for  $\text{TiO}_2$ /graphene composites.

in Figure 8b). Because the Fermi energy of graphene is much lower than the CB of  $\text{TiO}_2$ , the graphene can act as a sink for the photogenerated electrons. The excited electrons can be stored in the huge  $\pi$ – $\pi$  network of graphene nanosheets in the composites, which can retard the electron–hole recombination on  $\text{TiO}_2$ . This process facilitates effective interface charge separation and hinders carrier recombination.

The electron transfer between  $\text{TiO}_2$  and graphene nanosheets can be expressed as



On the other hand, the adsorbed HCHO molecule could directly transfer an electron to the chemical bonded  $\text{TiO}_2$ /graphene composite. DFT calculation results show that,<sup>29</sup> for HCHO molecule, the highest occupied molecular orbital (HOMO) is 2.5 eV below the Fermi level, and the lowest unoccupied molecular orbital (LUMO) is 0.6 eV above the Fermi level, so, as Figure 8b illustrates, the electron located at the LUMO of HCHO can transfer to graphene, and the holes remaining in the VB of  $\text{TiO}_2$  are reacted with the absorbed HCHO, as expressed by



The key to improving the oxidation efficiency for the Gx- $\text{TiO}_2$  composite is attributed to the IFCT effect, which decreases the possibility of recombination of electron–hole pairs, increases the number of holes participating in the photooxidation process, and thus enhances the photocatalytic



activity. The IFCT effect is experimentally supported by EIS, the gaseous phase photocurrent, and PL test results.

In the previous studies, EIS analysis has been commonly used to confirm the above proposition.<sup>22a,30</sup> Figure 9a shows

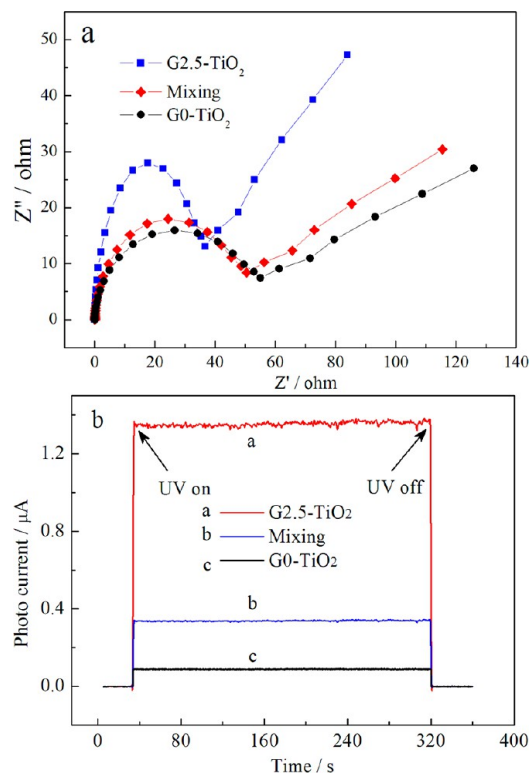


**Figure 9.** (a) EIS spectra and (b) gaseous phase photocurrent curves of G0-TiO<sub>2</sub>, G2.5-TiO<sub>2</sub>, and the mechanically mixed composite samples.

the EIS Nyquist plots of the as-prepared and the mechanically mixed TiO<sub>2</sub>/graphene nanocomposites with UV irradiation. The arc radius on the EIS Nyquist plot of G2.5-TiO<sub>2</sub> is the smallest of the three samples, and that of the Mixing sample is smaller than only the G0-TiO<sub>2</sub> sample. In the EIS Nyquist plot, the smaller semicircle size indicates an effective separation of photogenerated electron–hole pairs and fast interfacial charge transfer to the electron donor or acceptor.<sup>31</sup> Since the radius of the arc on the EIS spectra reflects the reaction rate occurring at the surface, it suggests that a more effective separation of photogenerated electron–hole pairs and a faster interfacial charge transfer occurs on the G2.5-TiO<sub>2</sub> photocatalyst under this condition. This result clearly indicates that the chemical combination of TiO<sub>2</sub> and graphene could effectively enhance the separation of photogenerated electron–hole pairs.

The EIS test was carried out under liquid conditions, which is clearly not the same as the gaseous degradation experiments. To further support the above proposition, the transient gaseous phase photocurrent responses were recorded for photoelectrodes consisting of pure TiO<sub>2</sub>, mechanically mixed, and chemically bonded TiO<sub>2</sub>/graphene nanocomposites under the same conditions as the photocatalytic reaction, that is, 200 ppm HCHO gas in air and UV LED irradiation. Figure 9b shows the  $I$ – $t$  curves for the three samples with UV irradiation. It is suggested that the photocurrent is determined mainly by the separation efficiency of the photogenerated electron–hole pairs within the photocatalyst. The photocurrent of the chemically

bonded composite (G2.5-TiO<sub>2</sub>) is enhanced  $\sim 15.3$  times that of pure TiO<sub>2</sub> (G0-TiO<sub>2</sub>), which indicates that the separation efficiency of photoinduced electrons and holes is improved through the electronic interaction between graphene nanosheets and TiO<sub>2</sub> nanoparticles. In addition, the photocurrent of the chemically bonded composite (G2.5-TiO<sub>2</sub>) is enhanced  $\sim 4.1$  times that of the mechanically mixed composite (Mixing), which is mainly due to the chemical interactions and the synergistic effect of graphene nanosheets and TiO<sub>2</sub> nanoparticles.

PL emission spectra resulting from the recombination of photoinduced charge transportation are powerful demonstrations of enhanced charge transportation and separation properties.<sup>11a</sup> PL signals for G0-TiO<sub>2</sub>, Mixing, and G2.5-TiO<sub>2</sub> under excitation at 325 nm are given in Figure 10. The lowest

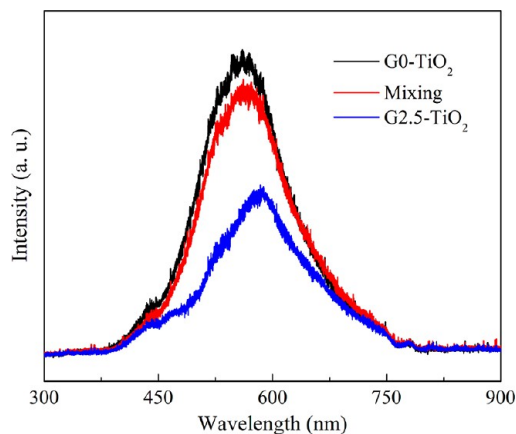


**Figure 10.** PL emission spectra of G0-TiO<sub>2</sub>, Mixing, and G2.5-TiO<sub>2</sub>.

PL intensity for G2.5-TiO<sub>2</sub> indicates the lowest recombination rate of photoinduced electron–hole pairs, which is consistent with the photocatalytic activity of the sample. In addition, Mixing also exhibits a slightly lower PL intensity than G0-TiO<sub>2</sub>, but its intensity is much higher than that of G2.5-TiO<sub>2</sub>. This is mainly attributed to the fewer defects in G2.5-TiO<sub>2</sub>, confirmed by the above Raman and XPS results. More importantly, this PL result demonstrates that only the TiO<sub>2</sub>/graphene composite with the chemical bonding interface can effectively facilitate charge transportation and separation, which is in good agreement with the results of EIS and gaseous phase photocurrent.

#### 4. CONCLUSION

In conclusion, TiO<sub>2</sub>/graphene nanocomposites with high photocatalytic activity were synthesized by a facile solvothermal approach at 200 °C for 10 h. The anatase TiO<sub>2</sub> nanocrystals were densely supported on graphene nanosheets with close interfacial contacts. Further characterization results indicate that the TiO<sub>2</sub> nanocrystals were chemically bonding with the graphene nanosheets, which is confirmed by the formation of the C–Ti bond in XPS. The chemically bonded nanocomposite (G2.5-TiO<sub>2</sub>) exhibits an enhancement of photocatalytic activity that is 2.6 times that of pure TiO<sub>2</sub>. On the basis of the EIS, gaseous phase photocurrent, and PL test results, this enhancement can be explained by the IFCT effect, which could provide a good spatial condition for charge transport from TiO<sub>2</sub> to graphene via the interfaces, decrease the possibility of

recombination of electron–hole pairs, and thus lead to higher photocatalytic activity.

## ■ ASSOCIATED CONTENT

### ● Supporting Information

Calculation method, four additional figures. This material is available free of charge via the Internet at <http://pubs.acs.org>.

## ■ AUTHOR INFORMATION

### Corresponding Author

\*Phone: +86-027-87559835; Fax: +86-027-87543778. E-mail: [dzweng@mail.hust.edu.cn](mailto:dzweng@mail.hust.edu.cn) (D.Z.), Phone/Fax: +86-027-87559836. E-mail: [csxie@mail.hust.edu.cn](mailto:csxie@mail.hust.edu.cn) (C.X.).

### Notes

The authors declare no competing financial interest.

## ■ ACKNOWLEDGMENTS

This work was supported by the National Basic Research Program of China (Grants Nos. 2009CB939702 and 2009CB939705) and Nature Science Foundation of China (Nos. 50772040 and 50927201). The authors are also grateful to the Analytical and Testing Center of Huazhong University of Science and Technology.

## ■ REFERENCES

- (1) Linsebigler, A.; Lu, G.; Yates, J. *Chem. Rev.* **1995**, *95*, 735.
- (2) (a) Inagaki, M.; Kojin, F.; Tryba, B.; Toyoda, M. *Carbon* **2005**, *43*, 1652. (b) Wang, Z.; Cai, W.; Hong, X.; Zhao, X.; Xu, F.; Cai, C. *Appl. Catal., B* **2005**, *57*, 223. (c) Divalentin, C.; Finazzi, E.; Pacchioni, G.; Selloni, A.; Livraghi, S.; Paganini, M.; Giamello, E. *Chem. Phys.* **2007**, *339*, 44.
- (3) (a) Mozia, S.; Toyoda, M.; Inagaki, M.; Tryba, B.; Morawski, A. J. *Hazard. Mater.* **2007**, *140*, 369. (b) Byrappa, K.; Dayananda, A. S.; Sajjan, C. P.; Basavalingu, B.; Shayan, M. B.; Soga, K.; Yoshimura, M. J. *Mater. Sci.* **2008**, *43*, 2348.
- (4) Kobayakawa, K.; Murakami, Y.; Sato, Y. J. *Photochem. Photobiol., A* **2005**, *170*, 177.
- (5) (a) Sun, L.; Zhao, Z.; Zhou, Y.; Liu, L. *Nanoscale* **2012**, *4*, 613. (b) Lambert, T. N.; Chavez, C. A.; Bell, N. S.; Washburn, C. M.; Wheeler, D. R.; Brumbach, M. T. *Nanoscale* **2011**, *3*, 188. (c) Li, M.; Tang, P. S.; Hong, Z. L.; Wang, M. Q. *Colloid Surf. A* **2008**, *318*, 285. (d) Li, M.; Hong, Z. L.; Fang, Y. N.; Huang, F. Q. *Mater. Res. Bull.* **2008**, *43*, 2179. (e) Li, M.; Zhou, S. F.; Zhang, Y. W.; Chen, G. Q.; Hong, Z. L. *Appl. Surf. Sci.* **2008**, *254*, 3762. (f) Khalid, N. R.; Ahmed, E.; Hong, Z. L.; Zhang, Y. W.; Ahmad, M. *Curr. Appl. Phys.* **2012**, *12*, 1485. (g) Khalid, N. R.; Ahmed, E.; Hong, Z. L.; Ahmad, M. *Appl. Surf. Sci.* **2012**, *263*, 254. (h) Khalid, N. R.; Hong, Z. L.; Ahmed, E.; Zhang, Y. W.; Chan, H.; Ahmad, M. *Appl. Surf. Sci.* **2012**, *258*, 5827. (j) Perera, S. D.; Mariano, R. G.; Vu, K.; Nour, N.; Seitz, O.; Chabal, Y.; Balkus, K. J., Jr. *ACS Catal.* **2012**, *2*, 949.
- (6) Chang, K.; Chen, W. *Chem. Commun.* **2011**, *47*, 4252.
- (7) (a) Wang, G.; Wang, B.; Park, J.; Yang, J.; Shen, X.; Yao, J. *Carbon* **2009**, *47*, 68. (b) Williams, G.; Seger, B.; Kamat, P. V. *ACS Nano* **2008**, *2*, 1487. (c) Zhang, H.; Lv, X.; Li, Y.; Wang, Y.; Li, J. *ACS Nano* **2010**, *4*, 380.
- (8) Wang, P.; Zhai, Y.; Wang, D.; Dong, S. *Nanoscale* **2011**, *3*, 1640.
- (9) Fan, W. Q.; Lai, Q. H.; Zhang, Q. H.; Wang, Y. J. *Phys. Chem. C* **2011**, *115*, 10694.
- (10) Choucair, M.; Thordarson, P.; Stride, J. A. *Nat. Nanotechnol.* **2008**, *4*, 30.
- (11) (a) Gao, F.; Zeng, D.; Huang, Q.; Tian, S.; Xie, C. *Phys. Chem. Chem. Phys.* **2012**, *4*, 613. (b) Huang, Q.; Zeng, D.; Li, H.; Xie, C. *Nanoscale* **2012**, *4*, 5651.
- (12) (a) Li, N.; Liu, G.; Zhen, C.; Li, F.; Zhang, L.; Cheng, H. *Adv. Funct. Mater.* **2011**, *21*, 1717. (b) Liu, G.; Yang, H. G.; Wang, X.; Cheng, L.; Lu, H.; Wang, L.; Lu, G. Q.; Cheng, H. J. *Phys. Chem. C* **2009**, *113*, 21784.
- (13) Malard, L. M.; Pimenta, M. A.; Dresselhaus, G.; Dresselhaus, M. S. *Phys. Rep.* **2009**, *473*, 51.
- (14) Lei, Y. K.; Liu, H. J.; Xiao, W. *Modell. Simul. Mater. Sci. Eng.* **2010**, *18*, 025004.
- (15) Wu, Z.; Dong, F.; Zhao, W.; Wang, H.; Liu, Y.; Guan, B. *Nanotechnology* **2009**, *20*, 235701.
- (16) Zhang, L.; Koka, R. V. *Mater. Chem. Phys.* **1998**, *57*, 23.
- (17) Jiang, G.; Lin, Z.; Chen, C.; Zhu, L.; Chang, Q.; Wang, N.; Wei, W.; Tang, H. *Carbon* **2011**, *49*, 2693.
- (18) Liu, G.; Wang, L.; Yang, H. G.; Cheng, H. M.; Lu, G. Q. M. J. *Mater. Chem.* **2010**, *20*, 831.
- (19) Makarova, O. V.; Rajh, T.; Thurnauer, M. C.; Martin, A.; Kempe, P. A.; Cropek, D. *Environ. Sci. Technol.* **2000**, *34*, 4797.
- (20) Wang, W.; Germanenko, I.; El-Shall, M. S. *Chem. Mater.* **2002**, *14*, 3028.
- (21) Murray, C.; Kagan, C.; Bawendi, M. *Annu. Rev. Mater. Sci.* **2000**, *30*, 545.
- (22) (a) Cao, A.; Liu, Z.; Chu, S.; Wu, M.; Ye, Z.; Cai, Z.; Chang, Y.; Wang, S.; Gong, Q.; Liu, Y. *Adv. Mater.* **2010**, *22*, 103. (b) Zhang, Y.; Tang, Z.; Fu, X.; Xu, Y. *ACS Nano* **2011**, *5*, 7426. (c) Wang, Y.; Shi, R.; Lin, J.; Zhu, Y. *Appl. Catal., B* **2010**, *100*, 179.
- (23) Liang, Y.; Wang, H.; Sanchez Casalongue, H.; Chen, Z.; Dai, H. *Nano Res.* **2010**, *3*, 701.
- (24) Zong, X.; Yan, H.; Wu, G.; Ma, G.; Wen, F.; Wang, L.; Li, C. J. *Am. Chem. Soc.* **2008**, *130*, 7176.
- (25) Xu, Y.; Schoonen, M. *Am. Mineral.* **2000**, *85*, 543.
- (26) Zhou, J.; Gu, Y.; Hu, Y.; Mai, W.; Yeh, P. H.; Bao, G.; Sood, A. K.; Polla, D. L.; Wang, Z. L. *Appl. Phys. Lett.* **2009**, *94*, 191103.
- (27) Muraoka, Y.; Takubo, N.; Hiroi, Z. *J. Appl. Phys.* **2009**, *105*, 103702.
- (28) (a) Tang, Y.; Lee, C.; Xu, J.; Liu, Z.; Chen, Z.; He, Z.; Cao, Y.; Yuan, G.; Song, H.; Chen, L.; Luo, L.; Cheng, H.; Zhang, W.; Bello, I.; Lee, S. *ACS Nano* **2010**, *4*, 3482. (b) Wang, X.; Zhi, L.; Mullen, K. *Nano Lett.* **2007**, *8*, 323.
- (29) Chi, M.; Zhao, Y. *Comput. Mater. Sci.* **2009**, *46*, 1085.
- (30) Gao, E.; Wang, W.; Shang, M.; Xu, J. *Phys. Chem. Chem. Phys.* **2011**, *13*, 2887.
- (31) Adachi, M.; Sakamoto, M.; Jiu, J.; Ogata, Y.; Isoda, S. J. *Phys. Chem. B* **2006**, *110*, 13872.